appropriate source dimension defined in terms of the second central moment of the Backus stress glut Γ(**r**,*t*) (*27*). The contours in Fig. 3 correspond to the $M_T^0 \sim L_c^3$ scaling relation of H. Kanamori and J. W. Given [*Phys. Earth Planet. Inter.* **27**, 8 (1981)] and the L_c^2 scaling of C. H. Scholz [*Bull. Seismol. Soc. Am.* **84**, 215 (1994)]. The latter scaling is thought to be more appropriate for the interplate, strike-slip events that dominate our sample.

15. H. Kanamori and G. S. Stewart, *Phys. Earth Planet. Inter.* **11**, 312 (1976); *ibid.* **18**, 167 (1979); E. A. Okal and L. M. Stewart, *Earth Planet. Sci. Lett.* **57**, 75 (1982); A. G. Prozorov and F. J. Sabina, *Geophys. J. R. Astron. Soc.* **76**, 317 (1984).
16. In a survey of anomalous free-oscillation excitations during the 2-year period 1978–1979, Beroza and Jordan (*27*) identified 14 slow earthquakes with $M_W \geq 6.2$; all were in oceanic lithosphere, and 11 were on oceanic transform faults.
17. The source time function is the time derivative of stress glut contracted against an average mechanism tensor $\hat{\mathbf{M}}$ and integrated over the source volume *V*:

$$f(t) = \frac{1}{\sqrt{2}} \int_V \dot{\Gamma}(\mathbf{r},t):\hat{\mathbf{M}}dV(\mathbf{r})$$

We assume that *f*(*t*) is a nonnegative function, which permits local slip reversals provided that the net slip at any time has a nonnegative projection onto $\hat{\mathbf{M}}$.

18. For transients beginning at t_0 and ending at t_∞, the source parameters are defined in terms of the moments

$$\mu_p = \int_{t_0}^{t_\infty} f(t)(t-t_0)^p dt, \ p = 0, 1, 2, \ldots$$

and associated central moments $\hat{\mu}_p$ (*3*): $M_T^0 = \mu_0$, $\Delta t_1 = \mu_1$, $\tau_c = 2\hat{\mu}_2^{1/2}$, and $\alpha = \hat{\mu}_3/2\mu_1{}^3$. The quantities M_T^0 and Δt_1 are the zero-frequency intercepts of $M_T(\omega)$ and $\Delta t(\omega)$, respectively, and τ_c and α are proportional to the downward curvatures of the spectra at $\omega = 0$. Equations 1 and 2 conform to these definitions, but they fix the higher moments ($p \geq 4$) to be special combinations of the low-order source parameters. Errors due to these choices of higher moments will not appreciably bias the estimates of the low-order parameters at frequencies less than $(t_\infty - t_0)^{-1}$. The source spectra were generally observed to vary slowly and smoothly out to 10 mHz, consistent with this criterion.

19. A typical example is the intermediate-magnitude (M_W = 6.4) Chile Transform earthquake of 12 November 1985, whose spectra are shown in Fig. 2. The centroid time shift determined from the phase-delay spectrum was $\Delta t_1 = 2.1 \pm 1.2$ s, essentially identical to the Harvard CMT value of 2.8 s. From 10 to 20 mHz, the amplitude spectrum was flat and extrapolated to a seismic moment of $(2.6 \pm 0.3) \times 10^{18}$ N-m, slightly smaller than the Harvard CMT value of 3.4×10^{18} N-m. The amplitude spectrum rose systematically below 10 mHz, however, indicating that this earthquake was a slow event; fitting Eq. 1 to these low-frequency values gave $M_T^0 = (4.8 \pm 0.4) \times 10^{18}$ N-m and $\tau_c = 39 \pm 4$ s. The integral of the likelihood function over the region of parameter space defined by inequalities 4 and 6 was less than 1%, so we rejected H_0 in favor of H_1 at the 99% CL.
20. R. Gaulon, J. Chorowicz, G. Vidal, B. Romanowicz, G. Roult, *Tectonophysics* **209**, 87 (1992). On the basis of the May–July 1990 earthquake sequence and supplementary field evidence, these investigators argued that the northwest-southeast–trending Aswa lineament is an active, left-lateral, intracontinental transform fault connecting the eastern and western branches of the East African Rift. They derived a Rayleigh-wave moment of 8.2×10^{19} N-m for the 20 May 1990 main shock, 50% larger than the Harvard CMT value and nearly twice the moment they computed from higher frequency body waves. These observations are consistent with the rapid roll-off in our amplitude spectrum at low frequencies (Fig. 2), which gave $M_T^0 = (7.7 \pm 0.6) \times 10^{19}$ N-m and $\tau_c = 52 \pm 4$ s. The Sudan earthquake thus plots in the slow-earthquake field of Fig. 3, and under H_0, its long duration is inconsistent at the 99% CL with its small centroid time shift, $\Delta t_1 = 8.4 \pm 1.2$ s (Fig. 4). The latter is in good agreement with the Harvard CMT value of 7.8 s.
21. The two normal-fault events (labeled N in Table 1) occurred on 8 July 1988, near Easter Island, and on 21 March 1988, in the Laptev Sea near the intersection of the Arctic mid-ocean ridge with the Asian continental slope. Three entries were designated as complex (labeled C), because they had moment tensors with significant compensated-linear-vector-dipole components; in most cases involving large moment release, such mechanisms are thought to be indicative of shear failures on multiple fault planes [C. Frohlich, *Science* **264**, 804 (1994)].
22. California earthquakes in our sample are Superstition Hills (24 November 1987) [D. C. Agnew and F. K. Wyatt, *Bull. Seismol. Soc. Am.* **79**, 480 (1989)], Loma Prieta (18 October 1989) [M. J. S. Johnston, A. T. Linde, M. T. Gladwin, *Geophys. Res. Lett.* **17**, 1777 (1990)], and Landers (28 June 1992) [M. J. S. Johnston, A. T. Linde, D. C. Agnew, *Bull. Seismol. Soc. Am.* **84**, 799 (1994)]. In the case of Landers, for example, the slight upward curvature of the phase-delay spectrum seen in Fig. 2 is consistent with the negative skewness of the source time function obtained by H. Kanamori, H.-K. Thio, D. Dreger, and E. Hauksson [*Geophys. Res. Lett.* **19**, 2267 (1992)] from waveforms recorded near the epicenter.
23. H. Kanamori and M. Kikuchi, *Nature* **361**, 714 (1993); S. F. Ide, F. Imamura, Y. Yoshida, K. Abe, *Geophys. Res. Lett.* **20**, 863 (1993).
24. "Quiet earthquake" is an infraseismic event that excites low-frequency (<5 mHz) free oscillations but does not produce detectable wave groups at teleseismic distances (*1*, *3*). This type of infraseismic source was postulated by Beroza and Jordan (*27*) to explain anomalous episodes of low-frequency mode excitation detected by the International Deployment of Accelerometers network during periods when no ordinary earthquake was observed. Experiments with synthetic seismograms for high-gain, broadband stations indicate that quiet earthquakes have characteristic durations greater than 200 s and amplitude spectra that roll off more rapidly than ω^{-3}.
25. I. S. Sacks, S. Suyehiro, A. T. Linde, J. A. Snoke, *Nature* **275**, 599 (1978); A. T. Linde, S. Suyehiro, S. Miura, I. S. Sacks, A. Takagi, *ibid.* **334**, 513 (1988); H. Kanamori, *Geophys. Res. Lett.* **16**, 1411 (1989).
26. P. G. Silver and T. H. Jordan, *J. Geophys. Res.* **88**, 3273 (1983).
27. G. C. Beroza and T. H. Jordan, *ibid.* **95**, 2485 (1990).

28. We thank P. Harabaglia and R. Cicerone for assistance and G. Ekström, J. Tromp, and E. Larson for the use of their unpublished phase-velocity maps. This research was sponsored by the National Science Foundation under grant EAR-9305081 and the National Aeronautics and Space Administration under grant NAG5-1905. P.F.I. was supported in part by grants from the Huber-Kudlich Stiftung and Sunburst Fonds.

29 July 1994; accepted 29 September 1994

Nanoscale Imaging of Molecular Adsorption

Heng Cai, Andrew C. Hillier,* Kevin R. Franklin, C. Craig Nunn,
Michael D. Ward*

In situ atomic force microscope observations were made of the adsorption of anions (1– or 2–) of the organic diacid 5-benzoyl-4-hydroxy-2-methoxybenzenesulfonic acid from aqueous solution onto the (0001) surface of hydrotalcite (HT), a layered clay. This adsorption process is believed to mimic the ion-exchange reactions that occur within the layers of HT and other layered clays. Atomic force microscope images of the (0001) surfaces of HT, acquired in aqueous solutions, reveal an ordered structure with respect to magnesium and aluminum atoms. In the presence of the anions, atomic force microscopy indicates pH-dependent adsorption onto the formally cationic HT surface. The anion coverage is governed by electroneutrality and steric interactions between the bulky anions within the adsorbed layer, whereas the orientation of the anions with respect to the HT surface is dictated by coulombic interactions and hydrogen bonding between the anion's sulfonate moiety and clay hydroxyl triads. These observations reveal that the reversible adsorption of molecular species can be examined directly by in situ atomic force microscopy, providing details of surface stoichiometry and adlayer symmetry on the local, molecular level.

Layered clays are of scientific and technological interest because of their use as ion-exchange materials (*1*), catalysts (*2*), antacids (*3*), catalytic supports (*4*), and modified electrodes (*5*). The observation that cationic clays preferentially adsorb one enantiomer when exposed to mixtures of L- and D-histidine has led to the suggestion that the stereoselective adsorption-desorption of molecules on clays may be related to the origin of chirality in living systems (*6*). Although conventional analytical methods have provided considerable insight into the reactivity and structure of layered clays, local characterization at the molecular level is lacking. In this report, we describe the use of atomic force microscopy (AFM) to visualize, in situ, the formation and structure of highly ordered adlayers of individual organic anions on the cationic surface of a layered clay, hydrotalcite (HT). These studies reveal the local structure and symmetry of adsorbed molecules, which may mimic the arrangement of these species when intercalated in HT.

Hydrotalcite, $Mg_6Al_2(OH)_{16}CO_3 \cdot 4H_2O$,

H. Cai and C. C. Nunn, Unilever Research U.S.–Edgewater Laboratory, 45 River Road, Edgewater, NJ 07020, USA.

A. C. Hillier and M. D. Ward, Department of Chemical Engineering and Materials Science, University of Minnesota, Amundson Hall, Minneapolis, MN 55455, USA.

K. R. Franklin, Unilever Research–Port Sunlight Laboratory, Quarry Road East, Bebington, Wirral L63 3JW, UK.

---

*To whom correspondence should be addressed.

which crystallizes as hexagonal plates (*7*) in the rhombohedral $R\bar{3}m$ space group, is representative of anionic clays (Fig. 1A) (*8*). These crystals consist of alternating cationic $Mg_6Al_2(OH)_{16}^{2+}$ and anionic $CO_3^{2-}\cdot 4H_2O$ layers (Fig. 1B). The cationic layers consist of metal hydroxide octahedra, which share edges to form densely packed, positively charged, brucite-like sheets terminated by hydroxyl groups and exhibiting hexagonal symmetry. The stoichiometry of HT dictates an overall 2+ charge per $Mg_6Al_2(OH)_{16}$ unit. The charge on these metal hydroxide sheets is compensated by the anions in the interstitial layers, which can be exchanged with other anions such as Cl^-, NO_3^-, and SO_4^{2-} under appropriate conditions (*9*, *10*).

The hydroxyl and metal atom positions within the HT (0001) layers exhibit a hexagonal motif with metal-metal and hydroxyl-hydroxyl spacings of 3.1 Å. The presence of two different metal atoms in the metal-hydroxide unit renders the hydroxyl sites inequivalent. A $Mg_6Al_2(OH)_{16}^{2+}$ layer that is ordered with respect to the metal atoms requires that 25% of the hydroxyl groups be bonded to three Mg atoms (Mg_3 sites) and the remaining 75% be bonded to two Mg atoms and one Al atom (Mg_2Al sites) (Fig. 1C). The Mg_3 sites of an ordered layer form a supercell with hexagonal symmetry and a lattice constant $a' = 6.2$ Å (Fig. 1C). The presence of these inequivalent sites would produce a surface corrugation in which the hydroxyl groups bonded to the Mg_3 sites extend above those bonded to the Mg_2Al sites, as deduced from the covalent radii of the metal atoms (Mg = 1.36 Å, Al = 1.18 Å).

Atomic force microscopy (*11*, *12*) of the (0001) face of HT (Fig. 2) supports ordering of the metal atoms in the HT metal-hydroxide layers. High-resolution AFM images acquired in aqueous solution reveal a hexagonal periodicity of contrast on the surface with a spacing of 6.4 ± 0.3 Å, in near agreement with $a' = 6.2$ Å for the ordered supercell (*13*). On the basis of the M–OH bond lengths, the bright regions in the images, which represent features closer to the AFM tip, are assigned to the Mg_3 hydroxyl groups. The irregular, nonspherical features may be a consequence of surface-bound water molecules, surface-bound carbonate anions, or the geometry of the AFM cantilever tip. Indeed, the influence of nonideal tip geometries on image characteristics has been suggested in a theoretical study (*14*) as well as in AFM images of montmorillonite and illite clays acquired in ambient air (*15*, *16*). Nevertheless, the AFM data clearly reveal a periodicity of contrast that is consistent with the presence of an ordered supercell in the cationic surface layer. Although some reports have implicated ordering of the Mg and Al atom positions, this has not been established unequivocally by x-ray analysis (*17*, *18*). Ordering has been suggested for the related clays $LiAl_2(OH)_7\cdot 2H_2O$ (*19*) and $LiAl_2(OH)_6 + X^-\cdot nH_2O$ (*18*) and for synthetic HT-like phases (*20*, *21*). The ordered arrangement of the (0001) HT surface revealed by AFM is most likely a consequence of coulombic interactions within the metal layer, as the average Al^{3+}–Al^{3+} distance is maximized in this configuration (*17*).

The cationic metal-hydroxide layers in HT exhibit two units of positive charge for every eight metal atoms [that is,

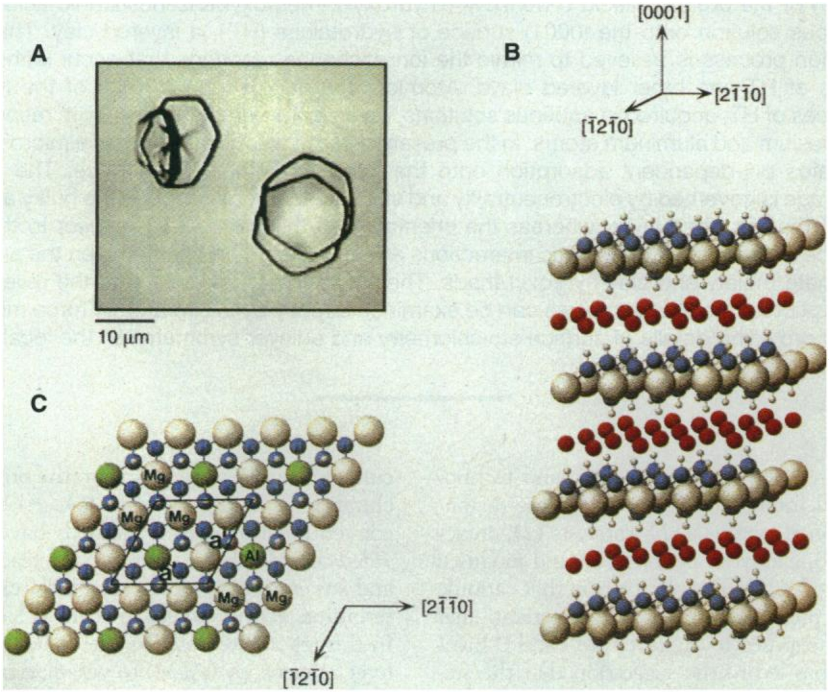

Fig. 1. (**A**) Hexagonal HT crystals adhering to a freshly cleaved mica substrate after spreading from a water suspension (photographed with an optical microscope). The (0001) plane is parallel to the mica substrate. (**B** and **C**) Structure of HT [$Mg_6Al_2(OH)_{16}CO_3\cdot 4H_2O$] as viewed normal to the ($\bar{1}$010) and (0001) planes. The ($\bar{1}$010) view in (B) illustrates the layered clay structure of HT, which consists of densely packed cationic $Mg_6Al_2(OH)_{16}^{2+}$ sheets separated by interstitial $CO_3^{2-}\cdot 4H_2O$ layers (each red sphere represents one-eighth of a $CO_3^{2-}\cdot 4H_2O$ unit). Oxygen atoms in the $Mg_6Al_2(OH)_{16}^{2+}$ sheets are blue. The cationic sheets exhibit hexagonal symmetry with respect to both the metal and the hydroxyl positions. In the ordered supercell depicted here, the hydroxyl groups are bonded to either Mg_3 or Mg_2Al sites. The hexagonal supercell, with $a' = 6.2$ Å, is indicated in (C).

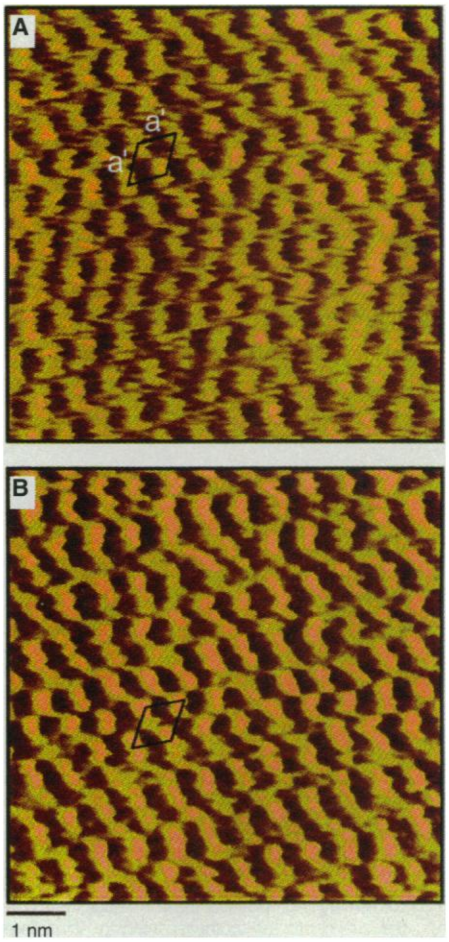

Fig. 2. AFM images of the (0001) face of a HT crystal in aqueous solution: (**A**) pH = 10.5; (**B**) pH = 6.6. The pH was adjusted by the addition of NaOH to 18-megohm deionized water. The AFM data reveal a contrast periodicity with hexagonal symmetry that can be described by a lattice constant of $a' = 6.4 \pm 0.3$ Å (the unit cell is overlaid on the AFM data). This value is nearly equivalent to the lattice constant of the ordered HT layer supercell ($a' = 6.2$ Å). The AFM images have been low pass–filtered.

$Mg_6Al_2(OH)_{16}{}^{2+}$], with the charge on the layers compensated by the interstitial anions. The HT sheet exposed at the outer crystal surface therefore has one unit of excess positive charge for every eight metal atoms because of incomplete charge compensation by the interstitial $CO_3{}^{2-}$ ions [these surfaces therefore are referred to as $Mg_6Al_2(OH)_{16}{}^{1+}$]. This excess surface charge must be compensated by anionic species adsorbed on the positively charged surface layers. If a medium containing more strongly binding anions is brought into contact with this surface, exchange at the surface will occur readily. It is likely that this event will mimic ion exchange associated with intercalation, a process important in applications for which clays are used (*9, 10*).

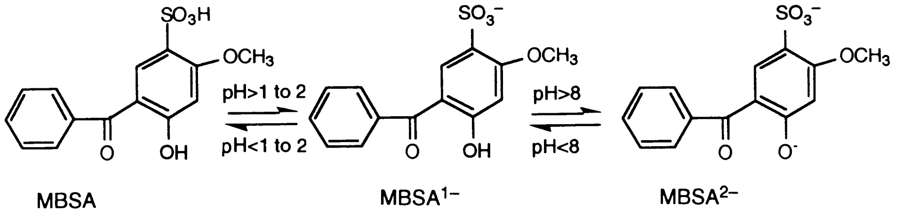

Fig. 3. Formation of $MBSA^{1-}$ and $MBSA^{2-}$.

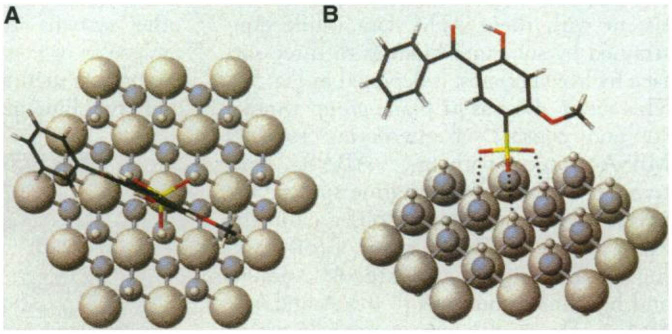

Fig. 4. Molecular model of the proposed orientation of $MBSA^{1-}$ or $MBSA^{2-}$ on the surface of HT as viewed (**A**) normal and (**B**) 30° off-parallel to the (0001) plane of HT. The putative hydrogen-bonding interaction between sulfonate oxygens and the hydroxyl triad sites is depicted. This orientation provides three favorable hydrogen-bonding interactions between the MBSA ion and the HT surface and allows for maximum coulombic interactions between the negatively charged sulfonate group and the positively charged HT metal layer. The Mg and Al atoms are depicted here as the same type for clarity.

In order to elucidate these processes locally on a molecular level, we used AFM to examine the adsorption of anions of 5-benzoyl-4-hydroxy-2-methoxybenzenesulfonic acid (MBSA) (*22*) on the HT (0001) surface (*23*). This acid, which has been shown to intercalate into HT (*24*), is of technological interest because of its use in cosmetics, pesticides, lithographic coatings, and ultraviolet screening agents (*25*). MBSA is also interesting for fundamental reasons as the presence of two acidic functionalities (Fig. 3) with relatively low pK_a values (pK_{a1} = 1 to 2, pK_{a2} = 8) makes it possible to examine the role of ionicity in adsorption on the $Mg_6Al_2(OH)_{16}{}^{1+}$ surface (*26*). In aqueous solutions adjusted to the appropriate pH, adsorption of either $MBSA^{1-}$ or $MBSA^{2-}$ will occur on the HT crystal surface to displace weakly bound ions and neutralize the excess charge residing on the surface (*27*). Molecular models suggest that the threefold symmetry and size of the sulfonate group on the MBSA anion are ideally suited for hydrogen-bonding interactions with the hydroxyl triads on the HT surface, which provide three hydrogen-bonding interactions per adsorbed MBSA anion (Fig. 4) (*28*). Weak hydrogen bonding between the hydroxide layers and the interstitial water molecules and anions is commonly accepted (*17, 21*). Close proximity of the negatively charged sulfonate group to the positively

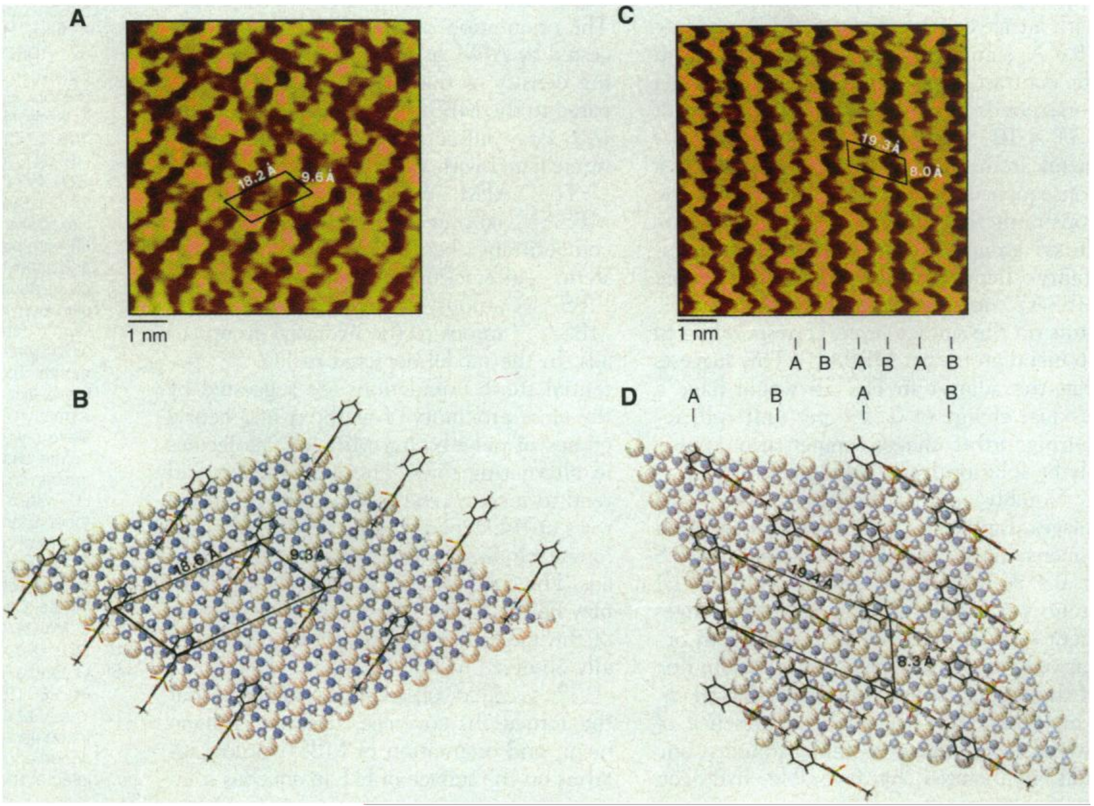

Fig. 5. (**A**) AFM image of the hexagonal (0001) face of HT in an aqueous solution containing $MBSA^{2-}$ (pH = 10.5). (**B**) Proposed structure of a molecular $MBSA^{2-}$ layer adsorbed on HT. (**C**) AFM image of the hexagonal (0001) face of HT in an aqueous solution containing $MBSA^{1-}$ (pH = 6.6). (**D**) Proposed structure of a molecular $MBSA^{1-}$ layer adsorbed on HT. Both packing motifs have *P*1 plane symmetry. The correspondence between the AFM data and the models is revealed by a comparison of the unit cells shown, the lattice constants determined from the AFM data ($MBSA^{2-}$: *a* = 9.6 Å and *b* = 18.2 Å; $MBSA^{1-}$: *a* = 8.0 Å and *b* = 19.3 Å) agreeing favorably with those of the models ($MBSA^{2-}$: *a* = 9.3 Å and *b* = 18.6 Å; $MBSA^{1-}$: *a* = 8.3 Å and *b* = 19.4 Å). The sulfonate groups of the $MBSA^{2-}$ anions were assumed to be hydrogen-bonded to hydroxyl triad sites as described in Fig. 4. The AFM images have been low pass–filtered.

charged HT surface layer would also tend to maximize attractive coulombic interactions. Hydrogen bonding and coulombic effects therefore would conspire to favor this orientation over others in which only van der Waals interactions between the MBSA anions and HT would be involved.

High-resolution AFM images of HT in the presence of a basic aqueous solution of 1.6 mM MBSA differ substantially from those observed in water containing no MBSA. In aqueous media at pH = 10.5, $MBSA^{2-}$ is the predominant species in solution. Under these conditions, the hexagonal motif of bare HT transforms into a periodic row structure (Fig. 5A). The periodicity of contrast conforms to a lattice with constants of $a = 9.6 \pm 0.4$ Å and $b = 18.2 \pm 0.4$ Å, based on average values determined from four independent HT images. If each major feature is assigned to an $MBSA^{2-}$ anion, the data are consistent with a monolayer coverage Γ of 1.06×10^{-10} mol cm^{-2}. This coverage is equivalent to one MBSA molecule per 18.9 metal atoms, based on the area per metal atom determined from the x-ray crystal structure of HT.

A molecular packing motif of $MBSA^{2-}$ molecules adsorbed on the HT surface that is consistent with the coverage deduced from the AFM data and takes into account sulfonate binding to hydroxyl group triads (either Mg_3 or Mg_2Al sites), while avoiding steric interactions between $MBSA^{2-}$ anions, is depicted in Fig. 5B. This ordered monolayer of $MBSA^{2-}$ anions has $p1$ plane symmetry and one molecule per unit cell, with lattice constants of $a = 9.3$ Å and $b = 18.6$ Å, similar to the values deduced from the contrast in the AFM image. This model corresponds to a monolayer coverage Γ of 1.11×10^{-10} mol cm^{-2} and a ratio of 18.0 metal atoms per $MBSA^{2-}$. This ratio is a consequence, as shown in Fig. 4, of the constraint that the dianion reside on hydroxyl group triads. However, electroneutrality dictates a stoichiometry of one $MBSA^{2-}$ for every two $Mg_6Al_2(OH)_{16}{}^{1+}$ units on the surface layer, corresponding to 16 metal atoms per $MBSA^{2-}$. This suggests that the adlayer in Fig. 5B would have a residual charge of 0.25+ per unit cell, requiring further charge compensation, possibly by solution hydroxide ions.

Notably, a small fraction of the AFM images displayed a compressed lattice with dimensions of $a = 9.2 \pm 0.4$ Å and $b = 17.8 \pm 0.4$ Å, which corresponds to 16 metal atoms per $MBSA^{2-}$. This adlayer arrangement satisfies electroneutrality but can occur only at the expense of specific binding of the anions to the hydroxyl group triads. This observation suggests the presence of two adlayer domains of similar stability, one that is dictated by favorable hydrogen bonding to hydroxyl group triads and the other by electroneutrality constraints.

Reducing the solution pH to values between pK_{a1} and pK_{a2} of MBSA produces a solution rich in the $MBSA^{1-}$ anion. In this case, electroneutrality supports a coverage of adsorbed $MBSA^{1-}$ molecules on HT that is double the coverage observed for $MBSA^{2-}$, resulting in a more densely packed surface layer of MBSA molecules. High-resolution AFM images of HT in a 1.6 mM solution of MBSA at pH = 6.6 (Fig. 5C) reveal a zigzag row structure with two major features contained in an area bounded by a lattice with constants of $a = 8.0 \pm 0.2$ Å and $b = 19.3 \pm 0.2$ Å. The area of the lattice contains 16.6 metal atoms, equivalent to 8.3 metal atoms per $MBSA^{1-}$ and a monolayer coverage Γ of 2.41×10^{-10} mol cm^{-2}.

A molecular packing motif that is consistent with these AFM data, while constrained by sulfonate binding to three surface hydroxyl groups, is depicted in Fig. 5D. This motif also has $p1$ plane group symmetry and consists of alternating rows of $MBSA^{1-}$ anions with an . . . ABAB. . . pattern, similar to the alternating spacing between the rows of contrast observed in the AFM data (*29*). The unit cell of this packing model contains two $MBSA^{1-}$ anions and has dimensions of $a = 8.3$ Å and $b = 19.4$ Å. The model corresponds to a coverage Γ of 2.36×10^{-10} mol cm^{-2}, which is equivalent to 8.5 metal atoms per $MBSA^{1-}$. This compares favorably to the ideal 8:1 ratio required for electroneutrality and the 8.3:1 ratio deduced from the AFM data. The orientation of the MBSA anions suggested by AFM, as well as the greater packing density of the $MBSA^{1-}$ adlayer compared to the $MBSA^{2-}$ adlayer, is consistent with x-ray diffraction data obtained for HT intercalated with these anions (*30*).

The AFM data observed for the $MBSA^{1-}$ adlayer most likely reflects the competition between electroneutrality, steric interactions between adjacent $MBSA^{1-}$ anions, and the binding of the $MBSA^{1-}$ anions to the hydroxyl group triads. In the model depicted in Fig. 5D, potential steric interactions are suggested by the close proximity of methoxy and benzyl groups of neighboring $MBSA^{1-}$ molecules in alternating rows. These contacts would tend to increase the spacing between these rows at the expense of ideal $MBSA^{1-}$ sulfonate binding to the surface hydroxyl triads. The competition between these factors may be the source of orientational disorder of the molecular features that is occasionally observed in AFM data.

These AFM observations indicate that the formation, coverage, packing arrangement, and orientation of MBSA anion adlayers on the surface of HT in aqueous solutions are governed by coulombic interactions between the MBSA anions and the positively charged clay surface, steric interactions between neighboring MBSA anions within the adlayer, and hydrogen-bonding interactions between the MBSA sulfonate group and hydroxyl group triads exposed at the HT surface layer. It is reasonable to suggest that the ordered structure of these adlayers mimics the structure of HT intercalate layers of MBSA (*30*). The presence of highly ordered intercalate layers would be in contrast with interstitial layers of inorganic anions, which are always considered to be disordered in these clays (*31*). These studies demonstrate the capability of in situ AFM methods for probing locally, on a molecular level, the formation and structure of molecular adlayers on well-defined substrates in their native environments. We anticipate that future AFM studies will extend this capability to other systems in which the formation of molecular aggregates on ordered surfaces is important, such as the growth of thin films and crystalline materials (*32*).

REFERENCES AND NOTES

1. P. K. Dutta and M. Puri, *J. Phys. Chem.* **93**, 376 (1989); H. C. B. Hansen and R. M. Taylor, *Clay Miner.* **26**, 311 (1991).
2. W. T. Reichle, S. Y. Kang, D. S. Everhardt, *J. Catal.* **101**, 352 (1986).
3. P. C. Schmidt, K. Benke, *Pharm. Acta Helv.* **63**, 188 (1988); Z. Kokot, *Pharmazie* **43**, 249 (1988); J. L. Fabregas and J. Cucala, *Int. J. Pharmacognosy* **52**, 173 (1989).
4. M. Rameswaran, E. G. Rightor, E. D. Dimotakis, T. J. Pinnaravaia, in *Proceedings of the International Congress on Catalysis* (North-Holland, Amsterdam, 1988), vol. 9, p. 783; H. van Olphen, *An Introduction to Clay Colloid Chemistry* (Wiley, New York, 1977).
5. K. Itaya, H.-C. Chang, I. Uchida, *Inorg. Chem.* **26**, 624 (1987); D. Ege, P. K. Ghosh, J. R. White, J. F. Equey, A. J. Bard, *J. Am. Chem. Soc.* **107**, 5644 (1985).
6. T. Ikeda, H. Amoh, T. Yasunaga, *J. Am. Chem. Soc.* **106**, 5772 (1984); A. Kachalski, *Nature* **228**, 636 (1970); E. T. Degens, J. Matheja, T. A. Jackson, *ibid.* **227**, 492 (1970); A. Yamagishi, *J. Phys. Chem.* **86**, 2472 (1982).
7. Hexagonal plate crystals of magnesium-aluminum HT with plate diameters of between 10 and 20 μm and aspect ratios of about 40 were prepared from a dilute aqueous solution containing 0.625 mmol of aluminum nitrate nonhydrate, 1.875 mmol of magnesium nitrate hexahydrate, and 31.25 mmol of urea, which was heated in a sealed bottle at 75°C for 1 month. The urea slowly hydrolyzes to provide both the basicity and the carbonate ions necessary for formation of the HT structure. The solid product was filtered, washed with warm water, and freeze-dried before characterization and use. X-ray powder diffraction showed the product to be a highly crystalline HT with a basal spacing of 7.6 Å. Chemical and thermal analysis results were consistent with the chemical composition $Mg_6Al_2(OH)_{16}CO_3 \cdot 4H_2O$.
8. R. Allmann, *Acta Crystallogr. Sect. B* **24**, 972 (1968); W. T. Reichle, *Solid State Ionics* **22**, 135 (1986); S. Miyata, *Clays Clay Miner.* **23**, 369 (1975).
9. S. Miyata, *Clays Clay Miner.* **31**, 305 (1983).
10. D. L. Bish, *Bull. Mineral.* **103**, 170 (1980).
11. G. Binnig, C. F. Quate, Ch. Gerber, *Phys. Rev. Lett.* **56**, 930 (1986).
12. The AFM experiments were performed with a Digital Instruments Nanoscope III scanning-probe microscope equipped with Nanoprobe cantilevers [Si_3N_4 integral tips with spring constants of 0.3 and 0.06

nm^{-1} (Park Scientific)]. Images were obtained in the constant-force mode with filters off, an integral gain of 3.0, a proportional gain of 7.0, and a look-ahead gain of 0.0. The "d" scan head was used, which has a maximum scan range of 12 μm by 12 μm by 4.4 μm. The scan rate of the tip during image acquisition ranged from 25 to 60 Hz, and the applied tip-sample force was maintained at $F_{tip} \leq 10$ nN in solution. The AFM experiments were performed in aqueous solutions with a fluid cell (Digital Instruments) consisting of a quartz body with ports for fluid entry and exit. Large single crystals of HT, about 10 to 20 μm in diameter, were allowed to adsorb from a water suspension onto a freshly cleaved mica substrate. The samples were then removed from the suspension and dried at 120°C for 1 hour. The mica substrate was then attached to a magnetic stainless steel AFM sample disk. We positioned the AFM tip above single HT crystals, using an optical microscope, before imaging.

13. The hexagonal symmetry and the lattice constant $a' = 6.2$ Å are also evident from Fourier analysis of the AFM data.
14. S. A. C. Gould, K. Burke, P. K. Hansma, *Phys. Rev. B* **40**, 5363 (1989).
15. J. Ganaes, H. Lindgreen, P. L. Hansen, S. A. C. Gould, P. K. Hansma, *Ultramicroscopy* **42–44**, 1428 (1992).
16. H. Hartman *et al., Clays Clay Miner.* **38**, 337 (1990).
17. G. W. Brindley and S. Kikkawa, *Am. Mineral.* **64**, 836 (1979).
18. C. L. Serna, J. L. Rendon, J. E. Iglesias, *Clays Clay Miner.* **30**, 180 (1982).
19. J. P. Thiel, C. K. Chiang, K. R. Poeppelmeier, *Chem. Mater.* **5**, 297 (1993).
20. M. C. Gastuche, G. Brown, M. M. Mortland, *Clay Miner.* **7**, 177 (1967); I. Pausch, H. H. Lohse, K. Schurmann, R. Allmann, *Clays Clay Miner.* **34**, 507 (1986).
21. G. Brown and M. C. Gastuche, *Clay Miner.* **7**, 193 (1967).
22. S. Budavari, Ed., *Merck Index* (Merck, Rahway, NJ, ed. 11, 1989), p. 1419.
23. The feasibility of using AFM to visualize, in situ, organic adsorbates was demonstrated for *tert*-butanol and *tert*-butylammonium cations on zeolite surfaces [A. L. Weisenhorn *et al., Science* **247**, 1330 (1990)].
24. S. W. Carr, K. R. Franklin, C. C. Nunn, J. J. Pasternak, I. Scott, European patent 557,089 (1993).
25. J. M. Knox, J. Guin, E. G. Cockerell, *J. Invest. Dermatol.* **29**, 435 (1957); J. M. Knox, A. C. Griffin, R. E. Hakim, *ibid.* **32**, 51 (1960).
26. The pK_a values listed for MBSA in this report were determined by the titration of 1.6 mmol of MBSA in aqueous solution with NaOH.
27. The absorption of MBSA^{1-} and MBSA^{2-} on HT has been verified by several independent analyses. X-ray photoelectron spectroscopy reveals the presence of MBSA in amounts approximating those expected for monolayer coverages. Infrared spectra indicate the presence of MBSA^{1-} or MBSA^{2-} on HT, which is infrared-transparent between 1000 and 1300 cm^{-1}. Adsorption was also confirmed from the depletion of MBSA^{1-} or MBSA^{2-} from solutions to which HT had been added.
28. We optimized the MBSA structure depicted in Fig. 4 using MOPAC and the CAChE molecular modeling program. The optimized structure compares favorably with that determined from single-crystal x-ray diffraction of guanidinium 5-benzoyl-4-hydroxy-2-methoxybenzenesulfonate (V. A. Russell and M. D. Ward, in preparation). The infrared spectral features of MBSA anions on HT in the region between 1000 and 1300 cm^{-1} are nearly identical to those observed for the guanidinium salt of MBSA^{1-} in which the sulfonate group is hydrogen-bonded to guanidinium protons and resides in a site of threefold C_{3v} symmetry. This arrangement is identical to that observed for a series of guanidinium sulfonates [V. A. Russell, M. C. Etter, M. D. Ward, *J. Am. Chem. Soc.* **116**, 1941 (1994)].
29. The . . . ABAB . . . pattern is also evident from Fourier analysis of the AFM data, which reveals two reciprocal space components along the reciprocal lattice vector a^* at 0.06 Å^{-1} and 0.12 Å^{-1}, consistent with the supercell depicted in Fig. 5C.
30. The coverages and orientation surmised from the AFM data, for both MBSA^{1-} and MBSA^{2-} adsorbates, are in agreement with previously reported chemical analyses and x-ray diffraction data of fully intercalated materials (*24*). Intercalation of MBSA^{1-} and MBSA^{2-} into the nitrate form of HT results in the expansion of the HT layers and the interatomic spacings of 21 and 13 Å, respectively. These values are consistent with the vertical orientation of the MBSA molecule, which has a height of about 11 Å. The larger interatomic spacing for MBSA^{1-} can be attributed to bilayer packing in which interdigitation of MBSA^{1-} ions on opposing HT layers is prohibited by the dense packing of the organic molecules. In contrast, the lower coverage of the MBSA^{2-} ions permits interdigitation of opposing adsorbate layers, leading to a smaller interatomic spacing.
31. L. Ingram and H. F. W. Taylor, *Mineral. Mag.* **26** (no. 280), 465 (1967).
32. L. Addadi *et al., Agnew. Chem.* **23**, 346 (1985); E. M. Landau, M. Levanon, L. Leiserowitz, M. Lahav, J. Sagiv, *Nature* **318**, 353 (1985); E. M. Landau *et al., Pure. Appl. Chem.* **61**, 673 (1989); P. W. Carter and M. D. Ward, *J. Am. Chem. Soc.* **115**, 11521 (1993).

33. H.C. thanks Y. Liu and S. Yang for assistance in AFM imaging. This research was supported by the National Science Foundation and the Center for Interfacial Engineering at the University of Minnesota. M.D.W. also received support from the National Science Foundation and the Office of Naval Research. The work of A.C.H. was supported under an Upjohn Fellowship during 1992–1993.

30 June 1994; accepted 28 September 1994

Wolves, Moose, and Tree Rings on Isle Royale

B. E. McLaren* and R. O. Peterson

Investigation of tree growth in Isle Royale National Park in Michigan revealed the influence of herbivores and carnivores on plants in an intimately linked food chain. Plant growth rates were regulated by cycles in animal density and responded to annual changes in primary productivity only when released from herbivory by wolf predation. Isle Royale's dendrochronology complements a rich literature on food chain control in aquatic systems, which often supports a trophic cascade model. This study provides evidence of top-down control in a forested ecosystem.

Terrestrial food chains of length three—plants, herbivores, and carnivores—are found throughout the temperate zone of the Northern Hemisphere, yet their establishment, pervasiveness, and stability are enigmatic subjects of debate among community ecologists (*1*). According to one hypothesis, depletion of green plants by herbivores occurs only in exceptional circumstances because carnivores usually control herbivores (*2*). However, systems in which increases in the density of a species at one trophic level accompany increases at higher, dependent trophic levels support a counterargument (*3*). The top-down (trophic cascade) model predicts that changes in density at one trophic level are caused by opposite changes in the next higher trophic level and that such inverse correlations cascade down a food chain. Accordingly, effects such as changes in primary productivity (the energy flow to plants) become noticeable only when higher, masking trophic levels are removed. After removal of carnivores from a three-level system, the control of density relationships is passed down the chain, to herbivores. The bottom-up model predicts that positive correlations occur between density changes at all trophic levels and especially between adjacent trophic levels, that changes in primary productivity affect higher trophic levels, and that extinction of the top trophic level does not change density patterns in lower levels.

We investigated food chain control in a large mammal system through observation of three trophic levels—a living system that is unlike two-level models of ungulate dynamics, which simulate the herbivore-plant interaction but are insensitive to parameter changes in a carnivore equation (*4*), and is also unlike models for ungulates that ignore the effects of vegetation change (*5*). Tree-ring analyses were used to characterize the interaction between an herbivore population and its winter forage in a system with an apparent cycle between predator and prey: the wolves (*Canis lupus*) and moose (*Alces alces*) in Isle Royale National Park, Michigan, the largest island (544 km^2) in Lake Superior (*6, 7*). Ring width in balsam fir (*Abies balsamea*), a tree that makes up 59% of winter moose diet (*8*), provided an index of the herbivore food base, even though it is not optimal forage for moose. We assumed that the annual wood accrual for fir was proportional to its foliar biomass, which is an approximate measure of standing forage crop.

Balsam fir covers a large area of Isle Royale (Fig. 1), although its relative abundance in the overstory has declined since the arrival of moose early in the 1900s, from 46% in 1848, to 13% in 1978, to ~5% today (*9*). The decline is attributed to the effect of moose herbivory; forests on small nearby islands that are less accessible to moose still have a large fir component (*10*). The lon-

---

Michigan Technological University, School of Forestry and Wood Products, Houghton, MI 49931, USA.

*To whom correspondence should be addressed.